


 Cite this: *Nanoscale*, 2021, **13**, 8514

Turning-on persistent luminescence out of chromium-doped zinc aluminate nanoparticles by instilling antisite defects under mild conditions†

 Xiaodan Huang,^{‡a,b} Xiaojun Wei,^{‡§a,b} Yan Zeng,^{‡b,c} Lihong Jing,^{‡*a} Haoran Ning,^{a,b} Xiaodan Sun,^{a,b} Yingying Li,^{a,b} Di Li,^d Yuanping Yi,^{‡c} and Mingyuan Gao,^{‡*a,b,e}

Spinel oxide nanocrystals are appealing hosts for Cr³⁺ for forming persistent luminescent nanomaterials due to their suitable fundamental bandgaps. Benefiting from their antisite defect-tolerant nature, zinc gallate doped with Cr³⁺ ions has become the most studied near-infrared (NIR) persistent luminescent material. However, it remains challenging to achieve persistent luminescence from its inexpensive analogs, e.g., zinc aluminate (ZnAl₂O₄). Because the radius difference of the cations in the latter system is bigger, it is intrinsically unfavorable for ZnAl₂O₄ to form Zn–Al antisite defects under mild conditions. Herein, we report a wet-chemical synthetic route for preparing Cr³⁺-doped ZnAl₂O₄ nanoparticles with long NIR persistent luminescence. It was demonstrated that methanol (MeOH) as an important component of the mixed solvent played a critical role in tailoring the morphology of the resulting ZnAl₂O₄:Cr nanocrystals. It could particularly drive the formation of antisite defects in the resulting coral-like nanoparticles bearing zinc-rich cores and zinc gradient peripheries. To disclose the effects of MeOH on the formation of antisite defects as well as particle morphologies, small molecules released during the pyrolysis of metal acetylacetonate precursors were analyzed by using gas chromatography-mass spectrometry. In combination with density functional theory (DFT) calculations, it was found that MeOH can effectively catalyze the thermolysis of metal acetylacetonate precursors, in particular Zn(acac)₂. Therefore, MeOH exhibits remarkable effects on the formation of antisite defects by balancing the decomposition rates of Zn(acac)₂ and Al(acac)₃ through its volume fraction in the reaction system. This work thus constitutes a hitherto less common strategy for achieving NIR persistent luminescence from Cr³⁺-doped ZnAl₂O₄ nanoparticles by engineering the cation defects under mild conditions.

Received 20th November 2020,

Accepted 1st April 2021

DOI: 10.1039/d0nr08267h

rsc.li/nanoscale

1. Introduction

Persistent luminescent nanoparticles have been considered as a promising class of emitters for background-free biomedical imaging as they are able to emit light after ceasing incident

excitation photons.^{1–7} Owing to the appropriate fundamental bandgaps, spinel oxides generally expressed as AB₂O₄ are appealing matrices for hosting Cr³⁺ ions for generating near-infrared (NIR) persistent luminescence with long afterglow duration.^{8–11} Normally, in the crystalline structure of a spinel

^aKey Laboratory of Colloid, Interface and Chemical Thermodynamics, Institute of Chemistry, Chinese Academy of Sciences, Bei Yi Jie 2, Zhong Guan Cun, Beijing 100190, China. E-mail: gaomy@iccas.ac.cn, jinglh@iccas.ac.cn; Fax: +86 10 8261 3214

^bSchool of Chemistry and Chemical Engineering, University of Chinese Academy of Sciences, Beijing 100049, China

^cKey Laboratory of Organic Solids, Institute of Chemistry, Chinese Academy of Sciences, 100190 Beijing, China

^dState Key Laboratory of Luminescence and Applications, Changchun Institute of Optics, Fine Mechanics and Physics, Chinese Academy of Sciences, 3888 Eastern South Lake Road, Changchun 130033, P. R. China

^eState Key Laboratory of Radiation Medicine and Protection, School for Radiological and Interdisciplinary Sciences, Collaborative Innovation Center of Radiation Medicine of Jiangsu Higher Education Institutions, Soochow University, Suzhou 215123, China

† Electronic supplementary information (ESI) available: (1) Thermal gravity curves of Al(acac)₃ and Zn(acac)₂. (2) TEM image together with the corresponding particle size histogram of ZAC-5 nanoparticles prepared through a seed-mediated growth. (3–4) Photoluminescence spectra and fluorescence excitation spectra of ZAC-2 and ZAC-5. (5) HRTEM image of ZAC-3 cube-like nanoparticles. (6) STEM-EDS elemental mapping of ZAC-5 nanoparticles. (7) Mass spectra of the species collected at a retention time of 1.45 min and 1.53 min, formed by methanol promoted decomposition of Zn(acac)₂ and Al(acac)₃. (8) Mechanism of Al–O–Zn bond formation catalyzed by MeOH. (9) The parameters for multi-exponentially fitting the decay curves. (10) Texture coefficients of ZAC-1 and ZAC-2 nanoparticles calculated based on the XRD diffraction peak positions. See DOI: 10.1039/d0nr08267h

‡ These authors contributed equally.

§ Present address: Department of Chemical Engineering, University of South Carolina, Columbia, SC 29208, USA.

host the divalent cation A occupies the tetrahedral site surrounded by four oxygen atoms, while trivalent cation B occupies the octahedral site surrounded by six oxygen atoms.^{12–14} However, when the positions of cations A and B are inverted, antisite defects are created. The antisite defects on the one hand introduce local electric fields that can effectively split the energetic level of the luminescent dopant, typically Cr³⁺ ions, to facilitate radiative recombination of charge carriers to generate persistent luminescence.^{15–17} On the other hand, the antisite defects serve as important energy storage centers before the electrons and holes finally recombine at the Cr³⁺ centers upon thermal activation.^{1,18} In this context, to effectively manipulate the density of antisite defects is paramount for improving the persistent luminescence and duration of AB₂O₄ type materials doped with Cr³⁺ ions.¹⁶

Spinel oxides such as ZnGa₂O₄, MgGa₂O₄, and Zn₃Ga₂Ge₂O₁₀ have been well-explored as hosts of Cr³⁺ ions for preparing NIR persistent luminescent materials as they naturally possess high levels of antisite defects,^{16–22} with a cation inversion ratio typically ranging from 3% to 44%, due to the comparable radius of cations A and B in these material systems.^{16,23} To date, the majority of the host materials are largely limited to gallate and gallogermanate oxides that are generally cost-prohibitive. Therefore, non-gallate materials are being explored as alternatives for hosting Cr³⁺ dopants. One of the potential candidates is zinc aluminate (ZnAl₂O₄) because it has a suitable optical bandgap of 3.8 eV and is also expected to be more stable owing to the higher dissociation energy (501.9 kJ mol⁻¹) of the Al–O bond than that of the Ga–O bond (374 kJ mol⁻¹), apart from its inexpensive nature. However, the intrinsically low level of antisite defects, generally below 1%,^{16,17,24,25} is apparently very unfavorable for zinc aluminate to serve as a matrix for the persistent luminescence of Cr³⁺. Therefore, the synthesis and optical properties of Cr³⁺-doped zinc aluminate nanocrystals are much less reported. Thus, effectively engineering the antisite defects becomes of utmost importance for achieving efficient persistent luminescence from zinc aluminate.

Some efforts have been devoted to increase the density of antisite defects in ZnAl₂O₄ materials. Through thermal treatment, the cation diffusion and redistribution in the solid solution state were promoted to increase the level of antisite defects. For example, ZnAl₂O₄ powder with inversion rates of 4.3%–17.1% was obtained through the so-called Pechini or coprecipitation method, followed by a calcination at 600–1350 °C.²⁴ The resulting concentration of antisite defects is expected to be strongly dependent on the thermal treatment history. Unfortunately, this method typically leads to particles of tens of micrometers with poor uniformities and morphologies, hardly suitable for biomedical applications. Apart from the thermal treatment approach, partly substituting the cationic ions of the matrix with other types of cationic ions is also effective for increasing the density of antisite defects.^{26–28} For example, by partly replacing Al³⁺ with Ge⁴⁺, bulky Zn_{1+x}Al_{2–2x}Ge_xO₄:Cr phosphors showing persistent luminescence decay time up to 120 h were obtained,²⁶ while substitut-

ing Mg²⁺ with Zn²⁺ was used to tune the emission profile of the persistent luminescence of nanosized Mg_{1–x}Zn_xAl₂O₄ particles doped with Cr³⁺ ions.²⁸ Although the cation doping introduces defects favorable for Cr³⁺ persistent emission, it makes the system too complicated to show the intrinsic effects of the antisite defects in ZnAl₂O₄ on the persistent luminescence of Cr³⁺. Nevertheless, the above-mentioned attempts at least suggest that ZnAl₂O₄ can accommodate defects for Cr³⁺ dopant ions to emit NIR persistent luminescence.

Herein, we report a wet-chemical synthesis of ZnAl₂O₄:Cr³⁺(ZAC) nanocrystals with improved persistent luminescence by pyrolyzing Zn(acac)₂, Al(acac)₃, and Cr(acac)₃ in a solvent mixture of octadecene (ODE) and oleic acid (OA) in the presence of methanol (MeOH). It was found that MeOH played a very critical role in tuning the size and morphology of the resulting nanoparticles. For example, simply by varying the amount of MeOH in the reaction system, the morphological transformation from coral-like nanostructures to nanocubes could easily be achieved, besides size tunability. Through systematic mechanistic studies, the impacts of MeOH on the pyrolysis of precursors, formation of antisite defects, and luminescence properties were elucidated by combining the experimental results with theoretical analysis.

2. Results and discussion

2.1. Synthesis of differently sized and shaped ZAC nanoparticles

The ZAC nanoparticles were solvothermally synthesized by pyrolyzing Zn(acac)₂, Al(acac)₃, and Cr(acac)₃ in a mixture of ODE and OA in the presence of MeOH at 220 °C. The transmission electron microscopy (TEM) images of the as-prepared nanoparticles together with the corresponding particle size distributions are shown in Fig. 1. Apparently, not only the size but also the morphology of the resulting ZAC nanocrystals can heavily be tuned by MeOH. For example, when the volume fraction of MeOH is increased from 1% to 2%, the average size of the resulting coral-like particles is decreased from 54.1 ± 5.2 nm (ZAC-1) to 28.4 ± 3.4 nm (ZAC-2). As the volume fraction of MeOH is further increased to 6% and 8%, the coral-like particles are transformed into cube- and quasicube-like particles with the particle size decreased down to 11.8 ± 1.5 nm (ZAC-3) and 7.4 ± 1.0 nm (ZAC-4), respectively. The selected-area electron diffraction patterns shown in insets of Fig. 1 suggest that the resulting particles are cubic phase ZnAl₂O₄ nanocrystals. It is worth mentioning that no ZAC nanoparticles could be obtained in the absence of MeOH although the precursors seem to decompose at 220 °C as shown in Fig. S1,† suggesting that MeOH plays a critical role in the formation of the cubic phase nanocrystals under the given experimental conditions.

Actually, similar size regulation effects were previously observed for ZnGa₂O₄:Cr³⁺ nanoparticles prepared through a comparable route.²⁹ It was found out that MeOH could accelerate the decomposition of Ga(acac)₃, because it can decrease the barrier of reaction by reducing the free energy of the polar

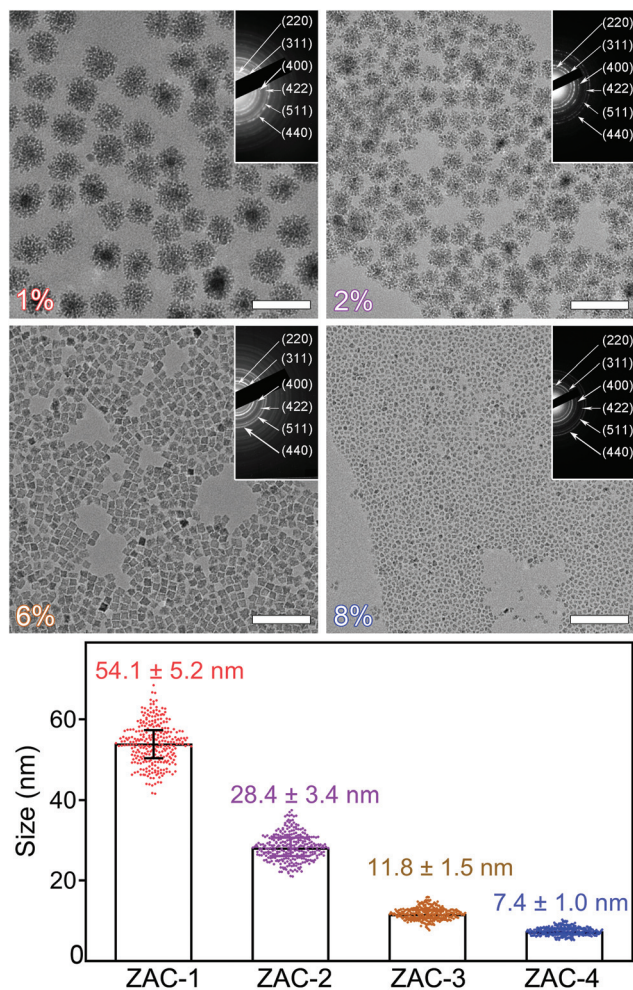


Fig. 1 TEM images and selected area electron diffraction patterns, labeled with lattice planes according to the standard card data for cubic ZnAl_2O_4 (JCPDS 82-1043), of ZAC nanoparticles prepared with varied MeOH volume fractions, *i.e.*, 1% (ZAC-1), 2% (ZAC-2), 6% (ZAC-3), and 8% (ZAC-4), together with the corresponding particle sizes and size distributions extracted from the TEM images (the embedded scale bars correspond to 100 nm).

transition state owing to its large dielectric constant ($\epsilon_{\text{MeOH}} = 32.6$), which is also applicable for explaining the strong size tuning effect of MeOH on the current $\text{ZnAl}_2\text{O}_4\text{:Cr}$ particles. But in contrast, MeOH was found to have a remarkable ability for tailoring the morphology of zinc aluminate nanoparticles to form coral-like particles apart from cube-like ones, which were not observed for $\text{ZnGa}_2\text{O}_4\text{:Cr}$ particles.

2.2. Optical properties of ZAC nanoparticles

The typical photoluminescence excitation (PLE) spectra, PL emission spectra, and PL decay curves of differently sized and shaped ZAC nanoparticles shown in Fig. 1 were recorded and are presented in Fig. 2. As shown in the left frame of Fig. 2a, the PLE signals monitored at 695 nm cover the region of 230–290 nm for coral-like ZAC-1 and ZAC-2 samples with excitation peaks locating at 258 nm, which can be attributed to the band-to-band transition of the host.^{1,2} The appearance of the excitation peak at 258 nm indicates that an efficient energy transfer process from the host to the Cr^{3+} dopants occurs in the coral-like nanoparticles. In contrast, the signals of cube-like ZAC-3 and ZAC-4 samples monitored at 689 nm cover a broader region, *i.e.*, 230–600 nm, showing three peaks at 310 nm, 397 nm, and 553 nm, corresponding to $^4\text{A}_2(\text{F}) \rightarrow ^4\text{T}_1(\text{F})$, $^4\text{A}_2(\text{F}) \rightarrow ^4\text{T}_1(\text{F})$, and $^4\text{A}_2(\text{F}) \rightarrow ^4\text{T}_2(\text{F})$ transitions of the Cr^{3+} dopants, respectively, separate from the peak at around 250 nm.^{8,30} In these cube-like nanoparticles, the direct excitation of Cr^{3+} ions upon light absorption at 300–600 nm apparently becomes competitive with the host excitation, which is obviously distinct from the PL excitation spectra of coral-like ZAC-1 and ZAC-2 samples. In the latter cases, the relatively low energy excitation peaks can be observed if the signal intensities are magnified by 100 times, indicating that the energy transfer from the host to Cr^{3+} is probably facilitated by the increased number of defects in the host lattice during the formation of the coral-like particles.^{2,31}

Although all these samples exhibit luminescence with similar profiles, the emission peak positions are different. For example, the emission peaks of coral-like ZAC-1 and ZAC-2 are

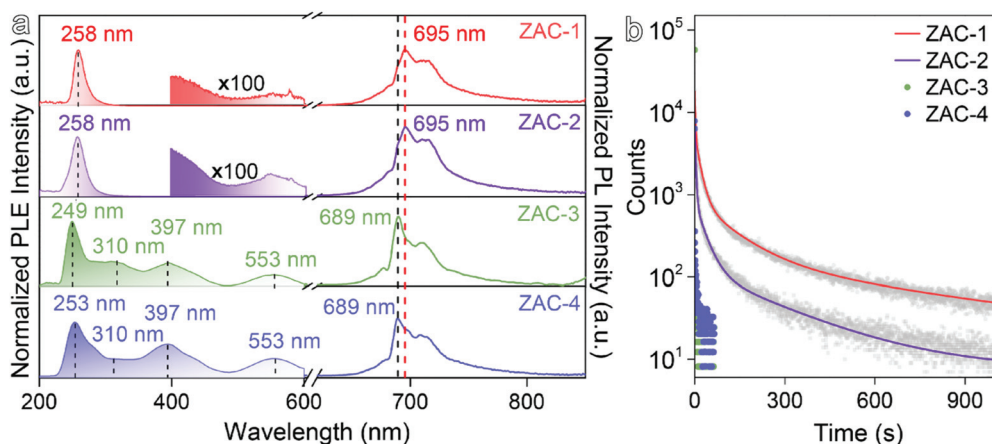


Fig. 2 Photoluminescence spectra together with the corresponding photoluminescence excitation spectra recorded upon excitation at 254 nm with a Xe lamp (a), and NIR persistent luminescence decay curves (b) of the ZAC 1–4 particles dispersed in cyclohexane.

centered at 695 nm under excitation at 254 nm, while the emission peaks of cube-like ZAC-3 and ZAC-4 are shifted to 689 nm. The former emission can be attributed to the N2-line emission of the Cr^{3+} dopant in an octahedron distorted by Zn–Al antisite defects through ${}^2\text{E} \rightarrow {}^4\text{A}_2$ transition, which in principle accounts for the long persistent luminescence of Cr^{3+} dopants,^{32,33} while the latter emission can be attributed to zero phonon line (known as R1-line) emission of a Cr^{3+} ion in an ideal undistorted octahedron through ${}^2\text{E} \rightarrow {}^4\text{A}_2$ transition.^{28,34,35} The above steady-state luminescence results suggest that the coral-like ZAC-1 and ZAC-2 have sufficient Zn–Al antisite defects to enable the N2-line emission from the Cr^{3+} dopants in the zinc aluminate matrix, in contrast to the cube-like ZAC-3 and ZAC-4. It has been previously revealed that the Li substitution of Al sites beside Na sites in $\text{NaAlSiO}_4\text{:Eu}$ facilitates defect formation that can effectively boost the emission intensity and tune the emission color.²⁷ Therefore, it can be concluded that a limited volume fraction of MeOH in the solvent is favorable for generating Zn–Al antisite defects, while further increasing the MeOH volume fraction is unfavorable for persistent luminescence.

The persistent luminescence from ZAC-1 and ZAC-2 was further confirmed by luminescence decay measurements. In contrast to ZAC-3 and ZAC-4, as shown in Fig. 2b, ZAC-1 and ZAC-2 present obvious persistent luminescence with long afterglow after excitation at 254 nm, while cube-like ones do not. According to the fitting results given in Table S1† based on multi-exponential functions, the average decay time of the luminescence centered at 695 nm is close to 295 s and 231 s for coral-like ZAC-1 and ZAC-2, respectively. The detailed fitting parameters further revealed that the lifetime of the fastest decay component of ZAC-1 was around 1.0 s, while the lifetime of the slowest decay component was up to 330.7 s. Moreover, the amplitude of the slowest decay component and the corresponding lifetime-amplitude product were around 36.2% and 87.4%, respectively. These data suggest that the slowest decay component is dominant and further indicate

that the storage and release of electrons captured by relatively deep traps are involved in the luminescence of the coral-like nanoparticles. In contrast, the luminescence of ZAC-3 and ZAC-4 decreased to the baseline immediately after the excitation was ceased. These transient emission spectroscopic studies demonstrate that the coral-like particles emit long afterglow persistent luminescence rather than the cube-like ones although their actual doping levels are nearly unchanged, *i.e.*, 0.28% for the coral-like ZAC-2 and 0.32% for the cube-like ZAC-3.

To rule out the possible size effects on the persistent luminescence, seed-mediated growth was employed to obtain nanoparticles with comparable size with persistent luminescent particles. For example, by using ZAC-3 as seeds, the particles of 28.9 ± 2.5 nm as shown in Fig. S2a† were obtained and denoted as ZAC-5. The XRD pattern shown in Fig. S2b† revealed that ZAC-5 had a zinc aluminate spinel structure according to the standard card data (JCPDS card, no. 82-1043). The PLE and PL spectra of ZAC-2 and ZAC-5 shown in Fig. S3 and S4† revealed that almost no persistent luminescence was presented by ZAC-5 although the particle size of ZAC-5 is very comparable with that of ZAC-2. Therefore, it is reasonable to deduce that ZAC-1 and ZAC-2 presenting persistent luminescence is not because they have bigger sizes.

2.3. Structural analysis of ZAC nanoparticles

To provide structural evidence for the formation of antisite defects inside ZAC-1 and ZAC-2 particles, FTIR investigations were performed. In an ideal ZnAl_2O_4 crystal, Al^{3+} ions occupying the octahedral sites are surrounded by six oxygen atoms (AlO_6).^{36,37} However, when it comes to a structure involving antisite defects, Al^{3+} ions are partly located in the tetrahedral sites surrounded by four oxygen atoms (AlO_4).^{38,39} The FTIR spectra of four ZAC 1–4 samples shown in Fig. 3a present two groups of signals in the region of $900\text{--}500\text{ cm}^{-1}$.⁴⁰ The presence of absorption bands at around 689 cm^{-1} and 563 cm^{-1} , which can be attributed to the symmetric stretching vibration

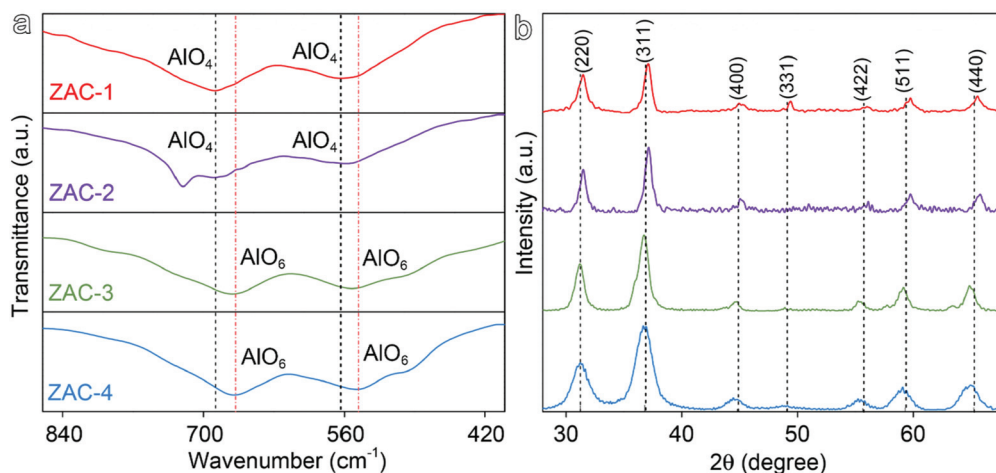


Fig. 3 FTIR spectra (a), and powder X-ray diffraction patterns together with JCPDS card data (82-1043) at the bottom (b) of the ZAC 1–4 nanoparticles.

and bending vibration of AlO_4 , suggests that ZAC-1 and ZAC-2 possess a certain number of AlO_4 structures that form the antisite defects.^{38,40} However, for ZAC-3 and ZAC-4, these two bands shift back to the normal positions for the symmetric stretching vibration and bending vibration of the AlO_6 form, *i.e.*, 668 cm^{-1} and 545 cm^{-1} , respectively. Therefore, ZAC-3 and ZAC-4 do not show observable persistent luminescence due to the lack of antisite defects.

The XRD results shown in Fig. 3b further reveal that the variation of MeOH volume fraction does not alter the zinc aluminate structure of the resulting particles. However, all diffraction peaks of ZAC-1 and ZAC-2 in comparison to standard data for zinc aluminate shift toward higher angles with diffraction peaks locating at high angles shifting more heavily. As the bond length (1.70 \AA) of Al–O in the AlO_4 tetrahedron is shorter than that (1.97 \AA) of Zn–O in the ZnO_4 tetrahedron, the partial substitution of Zn^{2+} with Al^{3+} to form the AlO_4 structure will reduce the tetrahedral bond length by 0.27 \AA .^{41,42} In contrast, substituting Al^{3+} with Zn^{2+} to form the ZnO_6 octahedron will increase the octahedral bond length by 0.19 \AA , given the fact that the bond length (2.11 \AA) of Zn–O in the ZnO_6 octahedron is longer than that (1.92 \AA) of Al–O in the AlO_6 octahedron.^{41,42} Thus, these two types of substitutions will lead to a net lattice contraction as the tetrahedron will experience a heavier distortion than the octahedron. Therefore, the shifting of the diffraction peaks to higher angles supports the partial substitution of Zn with Al in ZAC-1 and ZAC-2, but does not exclude the substitution of Al with Zn. Regarding ZAC-3 and ZAC-4, the diffraction peaks slightly shift to lower angles, probably because Al^{3+} is heavily replaced by Zn^{2+} ,⁴³ which finds supportive evidence from a Al/Zn ratio of $1.7 : 1$ determined through ICP-MS for the cube-like particles, *i.e.*, ZAC-3, which is largely away from the

stoichiometry of zinc aluminate. In contrast, the Al/Zn ratio is around $2 : 1$ for the coral-like particles, *i.e.*, ZAC-2, which supports the existence of antisite defects therein.

2.4. Structure and formation of coral-like nanoparticles

To show the detailed morphology of the resulting nanoparticles, HRTEM measurements were carried out to show the structural difference between the coral-like particles (Fig. 4a) and the cube-like particles (Fig. S5†). The results given in Fig. 4a reveal that the coral-like particles are formed by crystal-line domains showing a specific orientation that can quantitatively be described by a texture coefficient (TC) following the equation given below based on XRD results:

$$\text{TC}_{(hkl)} = \frac{N \left(\frac{I_{(hkl)}}{I_{o(hkl)}} \right)}{\sum_n \left(\frac{I_{(hkl)}}{I_{o(hkl)}} \right)} \quad (1)$$

where $I_{(hkl)}$ is the experimentally determined intensity of the diffraction peak from a specified plane (hkl), $I_{o(hkl)}$ is the standard intensity obtained from JCPDS cards, N is the total number of reflections, and n is the number of diffraction peaks. According to this equation, if $\text{TC}_{(hkl)} = 1$, the crystalline domains are randomly oriented, otherwise $\text{TC}_{(hkl)}$ is larger than 1. According to the data given in Fig. 3b, the $\text{TC}_{(311)}$ value calculated ranges from 1.26 for ZAC-1 to 1.31 for ZAC-2, confirming that the crystalline grains attached to each other *via* (311) planes to grow bigger.

To provide further compositional information for understanding the persistent luminescence of the coral-like particles, element mapping was carried out by using high-angle

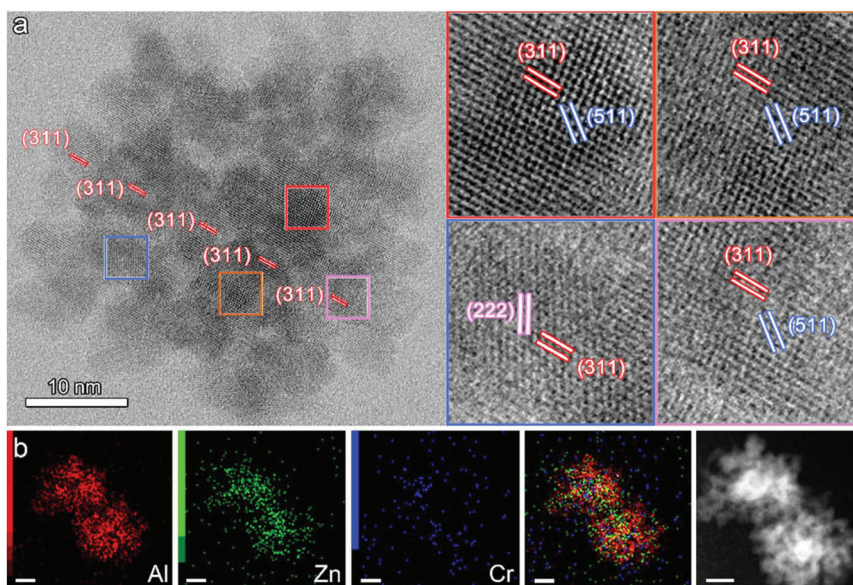


Fig. 4 HRTEM image of a typical coral-like ZAC nanoparticle together with its magnified parts shown within different color squares overlaid with the identification of crystal planes according to JCPDS card (82-1043) for ZnAl_2O_4 spinel (a), and STEM-EDS elemental mapping of twin coral-like nanoparticles (b) (the embedded scale bars correspond to 10 nm).

annular dark-field scanning transmission electron microscopy (HAADF-STEM). According to the detailed results given in Fig. 4b, Zn atoms are preferentially distributed in the central area of the selected twin particles, while Al atoms are rather evenly distributed throughout the whole particles. Therefore, it can be concluded that the persistent luminescent particles have a zinc-rich core and zinc gradient periphery. In other words, in the central area Al is prone to be replaced by Zn, while in the marginal area Zn is prone to be replaced by Al. Thus the formation of high level antisite defects is encouraged. In contrast, such a structure was not observed from the cube-like nanoparticles shown in Fig. S6.† It can therefore be concluded that the zinc-gradient structure is favorable for generating Zn–Al antisite defects that are responsible for the persistent luminescence of the coral-like ZAC particles.

2.5. Formation mechanism of antisite defects

The formation of the above-mentioned structure with a Zn-rich core and zinc gradient periphery implies that the thermal decomposition rates of Zn and Al precursors are dependent on the level of MeOH volume fraction. To demonstrate this hypothesis, the thermal decomposition kinetics of each metal acetylacetonate precursor were investigated by monitoring the generation of small molecules upon solvothermal decomposition in the presence of MeOH. The small molecules released

at different stages of the heating process were analyzed by GC-MS. As shown in Fig. 5a, two major types of GC signals are presented and can be attributed to acetone and methyl acetate, respectively, according to the MS signals at $m/z = 58$ and $m/z = 74$ as shown in Fig. S7.† In the previous well-documented investigations, acetone is one of the major small molecular products of the pyrolysis of metal acetylacetonates,^{44,45} while the presence of methyl acetate as a byproduct indicates that a possible reaction between MeOH and metal acetylacetonates takes place during the pyrolysis of metal acetylacetonate precursors. Therefore, the acetone signal can be used for monitoring the decomposition of the precursor, while the methyl acetate signal can be used for monitoring the involvement of MeOH in the current preparation. In this context, the signal evolution of acetone and methyl acetate, normalized according to the concentration of the acetylacetonate ligand, is plotted against the reaction time of the solvothermal process. As shown in Fig. 5b, the acetone signal appears at 0.25 h and then reaches the maximum value at 3 h with respect to Zn(acac)₂, indicating that the pyrolysis of the Zn precursor starts quickly after being heated to 220 °C and then takes place more vigorously during the initial 3 h of reaction. Thereafter, the pyrolysis reactions slow down according to the dramatically decreased acetone signal intensity. Although the acetone signal variation tendency is similar for Al(acac)₃, the signal

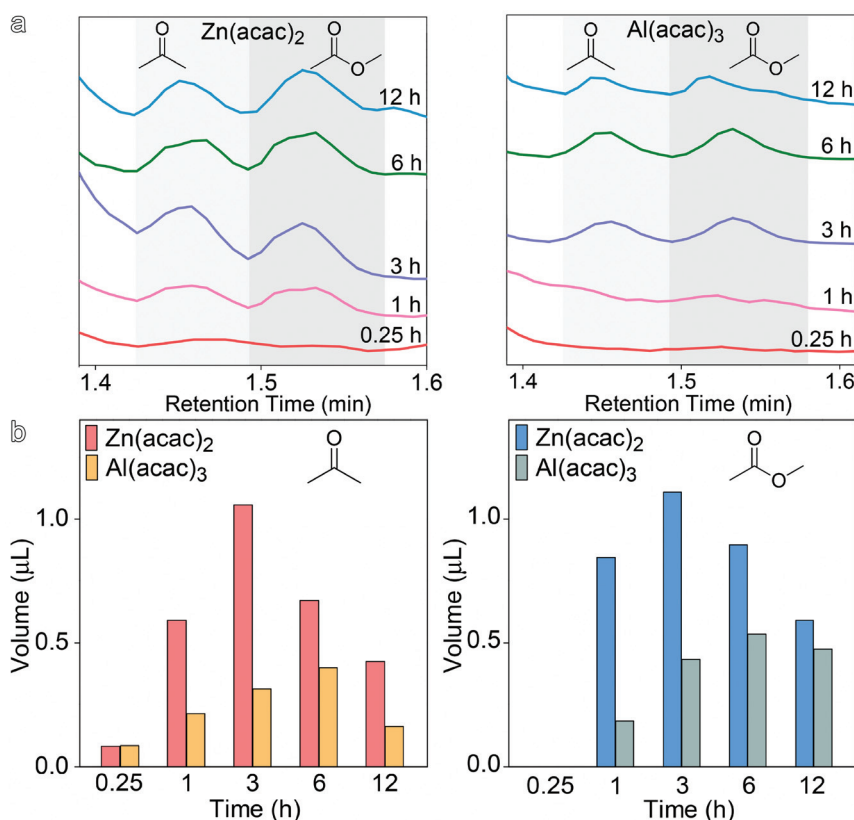


Fig. 5 Gas chromatograms of the pyrolyzed products of Zn(acac)₂ and Al(acac)₃ in the presence of MeOH collected at different reaction time points with the acetone and methyl acetate signals highlighted by light and dark gray, respectively (a), and the temporal amounts of acetone and methyl acetate normalized according to the initial concentration of the acetylacetonate ligand (b).

intensity increases much more slowly to reach the maximum value at 6 h post-pyrolysis, apparently falling behind the zinc counterpart. Regarding the formation of methyl acetate, the temporal signals given in the right frame of Fig. 5b present tendencies very similar to those of acetone generated from both systems, implying that MeOH may deeply be involved in the pyrolysis of the current metal precursors.

It merits mentioning that all results given in Fig. 5 are based on the volume fraction of MeOH for ZAC-3, because the volume fractions of MeOH for ZAC-1 and ZAC-2 were too low to generate detectable signals for acetone and methyl acetate, suggesting that MeOH can largely accelerate the decomposition of the metal precursors, particularly the Zn precursor. The unmatched decomposition rates of $\text{Zn}(\text{acac})_2$ and $\text{Al}(\text{acac})_3$ at a low MeOH level thus explain the zinc-rich core structure of ZAC-1 and ZAC-2. Probably because at a high level of MeOH the concentration of Al monomer becomes high enough, zinc rich structures are observed from ZAC-3 and ZAC-4, but the zinc-rich core is missing, partly due to the great decrease of the particle size.

In principle, as a strong polar reagent MeOH is reasonably expected to nucleophilically attack the electron-deficient carbonyl C atom in the acetylacetonate ligand of the metal precursors. The cracking of the C–C bond in consequence produces methyl acetate. It is assumed that the next hydrolysis step takes place through a nucleophilic attack of the M center by water molecules in the precursor hydrate, protons are transferred to enolates, and thus acetone is produced. The whole process leads to the formation of M–OH which represents the nucleating monomer units of ZnAl_2O_4 nanocrystals for forming Al–O–Zn bonds through the condensation reaction as shown in Fig. S8.† Therefore, in combination with the methyl

acetate signal evolution, it is reasonable to propose that MeOH binds with metal acetylacetonate precursors to catalyze their decompositions.

To provide further insights into the underlying molecular mechanism and particularly the thermodynamic aspects of the interactions between MeOH and metal acetylacetonate precursors, density functional theory (DFT) calculations were performed. Active sites including the central metal ion apart from the carbonyl moieties in acetylacetonate are also considered. The detailed theoretical calculation results shown in Fig. 6a reveal that the binding energy will be $-8.77 \text{ kJ mol}^{-1}$ if the hydroxyl oxygen of MeOH binds with the carbonyl C of the acetylacetonate ligand. However, if MeOH directly coordinates with the bivalent central metal ion, *e.g.*, Zn^{2+} , the binding energy goes further down to $-27.54 \text{ kJ mol}^{-1}$. It is in principle also possible for the hydroxyl hydrogen of MeOH to attack the carbonyl O site of the acetylacetonate ligand, then the binding energy goes to $-25.48 \text{ kJ mol}^{-1}$. All these results suggest that it is energetically favorable for polar MeOH to attack the zinc acetylacetonate through three different sites, *i.e.*, central metal ion, carbonyl carbon, and carbonyl oxygen moieties. The frontier molecular orbital calculations were also performed to support the different interaction patterns between MeOH and $\text{Zn}(\text{acac})_2$. As shown in Fig. 6b, once the $\text{Zn}(\text{acac})_2$ interacts with MeOH, the charge densities of the six-membered conjugated ring in the HOMO state are heavily redistributed regardless of the interaction sites. In consequence, the length of the C=O bond of the acetylacetonate ligand is elongated by 0.008 and 0.001 if O receives electrophilic attack and the C site receives nucleophilic attack by MeOH, respectively, as shown in Fig. 6c. The corresponding Mayer bond orders are decreased by 0.058 and 0.004, respectively, as shown in Fig. 6d. In con-

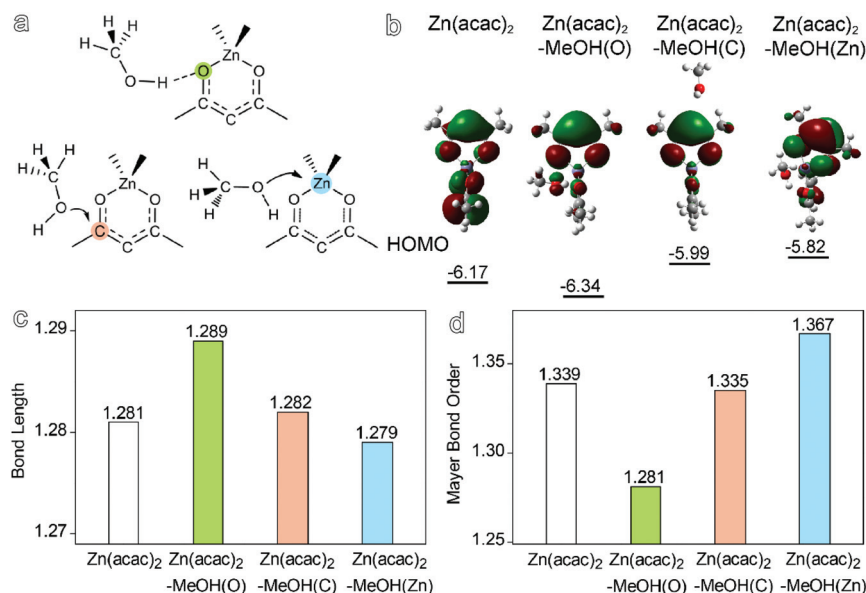


Fig. 6 Possible complexes formed using MeOH and $\text{Zn}(\text{acac})_2$ (a), HOMO orbitals and energy levels of $\text{Zn}(\text{acac})_2$ in the absence (left) or under attack by MeOH at O, C and Zn sites, respectively (b), together with the corresponding bond lengths (c), and Mayer bond orders (d) of the carbonyl groups upon interaction with MeOH.

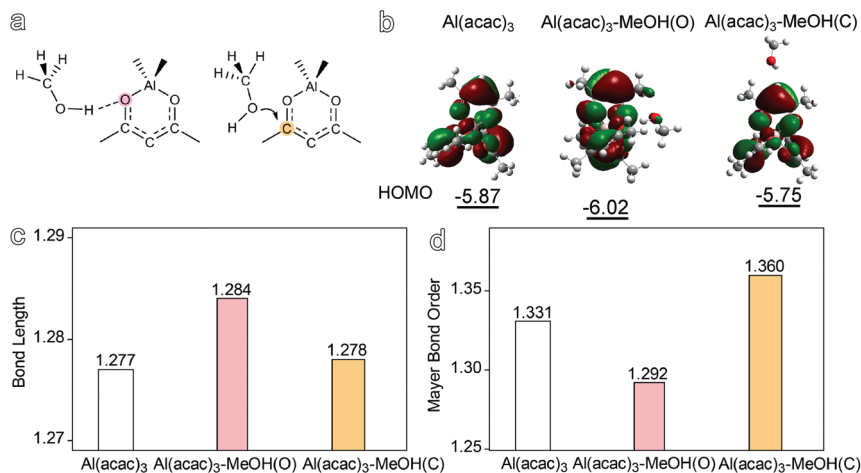


Fig. 7 Possible complexes formed using MeOH and $\text{Al}(\text{acac})_3$ (a), HOMO orbitals and energy levels of $\text{Al}(\text{acac})_3$ in the absence (left) or under attack by MeOH which attacks at the O and C sites, respectively (b), together with the corresponding bond lengths (c), and Mayer bond orders (d) of the carbonyl groups upon interaction with MeOH.

trast, if MeOH attacks the central Zn^{2+} ion, the $\text{C}=\text{O}$ bond length is shortened by 0.002, and the Mayer bond order is increased by 0.028. These theoretical calculations suggest that the $\text{C}=\text{O}$ bond strength of $\text{Zn}(\text{acac})_2$ is apparently weakened after being attacked by the MeOH molecule, particularly when the hydroxyl hydrogen of MeOH electrophilically attacks the carbonyl O site of $\text{Zn}(\text{acac})_2$. Therefore, it can be concluded that MeOH can catalyze the pyrolysis of the zinc precursor from thermodynamic aspects, which explains why no particles were obtained out of the reaction system in the absence of MeOH.

To further show the difference between the zinc and aluminum precursors with respect to thermolysis behaviors, DFT calculations on $\text{Al}(\text{acac})_3$ under attack by MeOH were also carried out. In general, it was found out that it is energetically unfavorable for MeOH to directly coordinate with the central Al^{3+} ions, probably due to the steric hindrance effects of the triple ligands.²⁹ However, MeOH can still attack the carbonyl moiety of $\text{Al}(\text{acac})_3$ through the C site and O site, respectively, as given in Fig. 7a and b. But the binding energies are largely different, *i.e.*, $-35.41 \text{ kJ mol}^{-1}$ for the electrophilic attack of the O site and $-8.02 \text{ kJ mol}^{-1}$ for the nucleophilic attack of the C site. Moreover, according to the variations of bond length and Mayer bond order given in Fig. 7c and d, the electrophilic attack of the O site of the $\text{Al}(\text{acac})_3$ is energetically much more favorable. Nevertheless, the catalyzing effect is weaker than that for $\text{Zn}(\text{acac})_2$, which is evidenced by the reduction of the Mayer bond order of the $\text{C}=\text{O}$ group, *e.g.*, 0.039 for $\text{Al}(\text{acac})_3$ *vs.*, 0.058 for $\text{Zn}(\text{acac})_2$. This difference further explains the existence of a zinc-rich core, which is observed when the volume fraction of MeOH is limited (*e.g.*, ZAC-1 and ZAC-2). However, when the volume fraction of MeOH is high enough, *e.g.*, ZAC-3 and ZAC-4, the pyrolysis kinetics of $\text{Al}(\text{acac})_3$ is accelerated to provide sufficient monomers. As a consequence, the resulting particles become much smaller and the particles with zinc-rich cores lose their forming foundation as well.

All the above evidence reveals that MeOH can largely regulate the pyrolysis of metal acetylacetonate precursors, as previously observed.²⁹ For example, by manipulating the decomposition of the $\text{Cr}(\text{acac})_3$ precursor, effective Cr^{3+} -doping was realized in achieving persistent luminescence from $\text{ZnGa}_2\text{O}_4:\text{Cr}^{3+}$ nanoparticles. Similarly but differently, MeOH plays a key role herein in balancing the thermolysis of $\text{Zn}(\text{acac})_2$ and $\text{Al}(\text{acac})_3$. When the volume fraction of MeOH is below 2%, the pyrolysis of $\text{Zn}(\text{acac})_2$ precursors is more kinetically and thermodynamically favorable than that of $\text{Al}(\text{acac})_3$, leading to the formation of coral-like nanoparticles with zinc-rich cores. Along with the quick consumption of the Zn precursor, the increased pyrolysis of the Al precursor enables the formation of the following zinc gradient structure at the periphery of the coral-like particles. Thus, the formation of antisite defects is remarkably encouraged. Therefore, the polar MeOH behaves like a molecular switch to give rise to persistent luminescence from ZAC nanoparticles under mild conditions.

3. Conclusion

In summary, coral-like $\text{ZnAl}_2\text{O}_4:\text{Cr}$ nanoparticles with a tunable size and long NIR afterglow luminescence were achieved *via* a MeOH-mediated wet-chemical synthesis. It was found out that properly balancing the decomposition rates of Zn and Al precursors with MeOH can effectively drive the formation of Zn–Al antisite defects in the coral-like $\text{ZnAl}_2\text{O}_4:\text{Cr}$ nanoparticles with zinc-rich cores and zinc gradient peripheries. This is because the pyrolysis of $\text{Zn}(\text{acac})_2$ is more kinetically favorable than that of $\text{Al}(\text{acac})_3$ in the presence of a limited amount of MeOH, which is also supported by theoretical analysis through DFT calculations. Under optimized conditions, the coral-like $\text{ZnAl}_2\text{O}_4:\text{Cr}$ nanoparticles obtained present reasonably long persistent luminescence. Nonetheless, further increasing the amount of MeOH in the reaction system

will also accelerate the decomposition of $\text{Al}(\text{acac})_3$, which is unfavorable for forming the zinc-rich core/zinc gradient periphery structure as well as the Zn–Al antisite defects under mild conditions. In summary, the current studies have demonstrated that by properly balancing the thermolysis of Zn and Al precursors, antisite defects that are essentially required for generating persistent luminescence out of zinc aluminate nanoparticles doped with Cr^{3+} can be created under mild conditions. Thus the current synthesis may provide an alternative to costly gallate and gallogermanate oxide hosts as persistent luminescent materials.

4. Experimental section

4.1. Chemicals

All the reagents were directly used as received, including Zn $(\text{acac})_2 \cdot x\text{H}_2\text{O}$ (97%, Aldrich) ($x \sim 5$), $\text{Al}(\text{acac})_3$ (99.99%, Aladdin), $\text{Cr}(\text{acac})_3$ (97%, Aldrich), octadecene (90%, Aldrich), oleic acid (90%, Aldrich), cyclohexane (99.5%, Beijing Chemical Works), methanol and ethanol (99.9%, Xilong Chemical).

4.2. Characterization

Transmission electron microscopy (TEM) images were recorded with a HT-7700 electron microscope operating at an accelerating voltage of 100 kV. Electron diffraction (ED) patterns and high resolution TEM (HRTEM) were recorded with a JEM 2100F electron microscope operating at an accelerating voltage of 200 kV. The particle size was measured with Image J by averaging at least 300 particles per sample. A high-angle annular dark-field (HAADF-STEM) image and energy-dispersive spectroscopy (EDS) elemental mapping images were taken from a JEM ARM200F spherical aberration-corrected transmission electron microscope operating at an accelerating voltage of 200 kV. Powder X-ray diffraction (XRD) patterns of the particle samples were recorded on a Rigaku D/Max-2500 diffractometer with the step size of 1° min^{-1} under $\text{Cu K}\alpha_1$ radiation ($\lambda = 1.54056 \text{ \AA}$). The composition of the nanoparticles was determined by inductively coupled plasma-mass spectrometry (ICP-MS) on a Thermo iCAP RQ after they were degraded in a full automatic microwave with a mixture of concentrated HNO_3 and hydrogen peroxide. The steady-state luminescence spectra, decay curves, and the absolute photoluminescence QY of the particles dispersed in cyclohexane were measured using a steady state/transient FLS980 fluorescence spectrometer (Edinburgh Instruments, UK) equipped with an integrating sphere under excitation at 254 nm. The decay curves were recorded after the particle sample was excited for 5 min. Fourier transform infrared (FTIR) spectra were recorded at room temperature on a Bruker TENSOR-27 FT-IR spectrometer. Thermo gravimetric analysis (TGA) was performed on a NETZSCH TG209F3 thermogravimetric analyzer. Gas chromatography-mass spectrometry (GC-MS) studies were carried out using a GCMS-QP2010Ultra in toluene.

4.3. Computational method

To elucidate the reaction mechanism, the molecular geometries of the isolated metal acetylacetonate, *e.g.*, $\text{Zn}(\text{acac})_2$, $\text{Al}(\text{acac})_3$, MeOH molecules, and all resulting complexes were optimized by density functional theory (DFT) calculations at the B3LYP/6-31G(d,p) (nonmetal atoms) + def2-TZVP (metal atoms) level in the gas phase.⁴⁶ Then, the vibrational frequency analysis at the same level is applied to confirm that the optimized geometries are really the minimum points on the potential energy surfaces. Based on the DFT-optimized geometries, the Mayer bond orders were calculated by using the Multiwfn program to show the variation of bond strength of acetylacetonate under attack by MeOH.⁴⁷

4.4. Synthesis of $\text{ZnAl}_2\text{O}_4 \cdot \text{Cr}^{3+}$ nanoparticles

$\text{ZnAl}_2\text{O}_4 \cdot \text{Cr}^{3+}$ (ZAC) nanoparticles were synthesized as follows. Typically, 0.179 g of $\text{Zn}(\text{acac})_2 \cdot x\text{H}_2\text{O}$ (0.5 mmol), 0.343 g of $\text{Al}(\text{acac})_3$ (1 mmol), and 1.047 mg of $\text{Cr}(\text{acac})_3$ (0.003 mmol) were dissolved in $(50-x)$ mL of a mixture formed using $(30-x)$ mL of ODE and 20 mL of OA under stirring at 80 °C. After the solution was cooled to approximately 40 °C, x mL (*e.g.*, 0.5, 1.0, 3.0, 4.0 mL) of MeOH was added under stirring. The resulting mixture was then transferred into a Teflon lined autoclave (100 mL) and treated at 220 °C for 24 h. After cooling naturally to room temperature, the resulting ZAC nanoparticles were precipitated, isolated through centrifugation, then washed alternately with ethanol and cyclohexane for three cycles, and finally re-dispersed in cyclohexane for further characterization. MeOH was found to play a critical role in the particle size and shape. A seed-mediated growth was also adopted for growing bigger ZAC nanoparticles. Typically, 0.1 mmol of ZAC nanoparticles were dissolved in a mixture comprised of $(30-x)$ mL of ODE, 20 mL of OA and x mL of MeOH containing 0.5 mmol Zn $(\text{acac})_2 \cdot x\text{H}_2\text{O}$, 1 mmol $\text{Al}(\text{acac})_3$, and 0.003 mmol $\text{Cr}(\text{acac})_3$ precursor. The reaction mixture was processed according to the same procedures mentioned above to further increase the size of the nanoparticles.

Conflicts of interest

The authors declare no conflicts of interest.

Acknowledgements

The authors acknowledge the financial support from the National Key Research Program of China (2018YFA0208800), NSFC (81720108024, 81530057, and 81671755), Youth Innovation Promotion Association CAS (2018042), CAS-VPST Silk Road Science Fund 2019 (GJHZ201963), and State Key Laboratory of Luminescence and Applications (SKLA-2019-01).

References

- 1 T. Maldiney, A. Bessiere, J. Seguin, E. Teston, S. K. Sharma, B. Viana, A. J. J. Bos, P. Dorenbos, M. Bessodes, D. Gourier, D. Scherman and C. Richard, *Nat. Mater.*, 2014, **13**, 418–426.
- 2 A. Abdulkayum, J.-T. Chen, Q. Zhao and X.-P. Yan, *J. Am. Chem. Soc.*, 2013, **135**, 14125–14133.
- 3 Z. Li, Y. Zhang, X. Wu, L. Huang, D. Li, W. Fan and G. Han, *J. Am. Chem. Soc.*, 2015, **137**, 5304–5307.
- 4 Z. H. Zhou, W. Zheng, J. T. Kong, Y. Liu, P. Huang, S. Y. Zhou, Z. Chen, J. L. Shi and X. Y. Chen, *Nanoscale*, 2017, **9**, 6846–6853.
- 5 J. T. Xu, A. Gulzar, P. P. Yang, H. T. Bi, D. Yang, S. L. Gai, F. He, J. Lin, B. G. Xing and D. Y. Jin, *Coord. Chem. Rev.*, 2019, **381**, 104–134.
- 6 Q. Miao, C. Xie, X. Zhen, Y. Lyu, H. Duan, X. Liu, J. V. Jokerst and K. Pu, *Nat. Biotechnol.*, 2017, **35**, 1102–1110.
- 7 S.-K. Sun, J.-C. Wu, H. Wang, L. Zhou, C. Zhang, R. Cheng, D. Kan, X. Zhang and C. Yu, *Biomaterials*, 2019, **218**, 119328.
- 8 Z. Pan, Y.-Y. Lu and F. Liu, *Nat. Mater.*, 2012, **11**, 58–63.
- 9 J. Wang, Q. Q. Ma, Y. Q. Wang, H. J. Shen and Q. Yuan, *Nanoscale*, 2017, **9**, 6204–6218.
- 10 B. Struve and G. Huber, *Appl. Phys. B: Photophys. Laser Chem.*, 1985, **36**, 195–201.
- 11 L. S. Forster, *Chem. Rev.*, 1990, **90**, 331–353.
- 12 N. Pellerin, C. Dodane-Thiriet, V. Montouillout, M. Beauvy and D. Massiot, *J. Phys. Chem. B*, 2007, **111**, 12707–12714.
- 13 K. E. Sickafus, J. M. Wills and N. W. Grimes, *J. Am. Ceram. Soc.*, 1999, **82**, 3279–3292.
- 14 V. Sreeja, T. S. Smitha, D. Nand, T. G. Ajithkumar and P. A. Joy, *J. Phys. Chem. C*, 2008, **112**, 14737–14744.
- 15 A. De Vos, K. Lejaeghere, D. E. P. Vanpoucke, J. J. Joos, P. F. Smet and K. Hemelsoet, *Inorg. Chem.*, 2016, **55**, 2402–2412.
- 16 N. Basavaraju, K. R. Priolkar, D. Gourier, S. K. Sharma, A. Bessiere and B. Viana, *Phys. Chem. Chem. Phys.*, 2015, **17**, 1790–1799.
- 17 N. Basavaraju, K. R. Priolkar, D. Gourier, A. Bessiere and B. Viana, *Phys. Chem. Chem. Phys.*, 2015, **17**, 10993–10999.
- 18 A. Bessiere, S. K. Sharma, N. Basavaraju, K. R. Priolkar, L. Binet, B. Viana, A. J. J. Bos, T. Maldiney, C. Richard, D. Scherman and D. Gourier, *Chem. Mater.*, 2014, **26**, 1365–1373.
- 19 Y. J. Li and X. P. Yan, *Nanoscale*, 2016, **8**, 14965–14970.
- 20 Q. Y. Bai, S. L. Zhao, L. Guan, Z. J. Wang, P. L. Li and Z. Xu, *Cryst. Growth Des.*, 2018, **18**, 3178–3186.
- 21 H. H. Liu, F. Ren, H. Zhang, Y. B. Han, H. Z. Qin, J. F. Zeng, Y. Wang, Q. Sun, Z. Li and M. Y. Gao, *J. Mater. Chem. B*, 2018, **6**, 1508–1518.
- 22 X. Lv, N. Chen, J. Wang and Q. Yuan, *Sci. China Mater.*, 2020, **63**, 1808–1817.
- 23 E. Finley, M. W. Gaultois and J. Brgoch, *Phys. Chem. Chem. Phys.*, 2019, **21**, 19349–19358.
- 24 L. Cornu, M. Gaudon and V. Jubera, *J. Mater. Chem. C*, 2013, **1**, 5419.
- 25 E. Finley and J. Brgoch, *J. Mater. Chem. C*, 2019, **7**, 2005–2013.
- 26 Y. Zhang, R. Huang, H. Li, D. Hou, Z. Lin, J. Song, Y. Guo, H. Lin, C. Song, Z. Lin and J. Robertson, *Acta Mater.*, 2018, **155**, 214–221.
- 27 M. Zhao, Z. Xia, X. Huang, L. Ning, R. Gautier, M. S. Molokeev, Y. Zhou, Y.-C. Chuang, Q. Zhang, Q. Liu and K. R. Poeppelmeier, *Sci. Adv.*, 2019, **5**, eaav0363.
- 28 H. G. S. Karthik, S. G. Menon, N. D. Hebbar, K. S. Choudhari, C. Santhosh and S. D. Kulkarni, *Mater. Res. Bull.*, 2019, **111**, 294–300.
- 29 X. Wei, X. Huang, Y. Zeng, L. Jing, W. Tang, X. Li, H. Ning, X. Sun, Y. Yi and M. Gao, *ACS Nano*, 2020, **14**, 12113–12124.
- 30 Y. Wang, C. X. Yang and X. P. Yan, *Nanoscale*, 2017, **9**, 9049–9055.
- 31 Z. Zhou, W. Zheng, J. Kong, Y. Liu, P. Huang, S. Zhou, Z. Chen, J. Shi and X. Chen, *Nanoscale*, 2017, **9**, 6846–6853.
- 32 D. Zhang, Y. H. Qiu, Y. R. Xie, X. C. Zhou, Q. R. Wang, Q. Shi, S. H. Li and W. J. Wang, *Mater. Des.*, 2017, **115**, 37–45.
- 33 D. Zhang, Q. Guo, Y. Ren, C. Wang, Q. Shi, Q. Wang, X. Xiao, W. Wang and Q. Fan, *J. Sol-Gel Sci. Technol.*, 2018, **85**, 121–131.
- 34 V. Singh, R. P. S. Chakradhar, J. L. Rao and H.-Y. Kwak, *J. Mater. Sci.*, 2011, **46**, 2331–2337.
- 35 S. G. Menon, D. N. Hebbar, S. D. Kulkarni, K. S. Choudhari and C. Santhosh, *Mater. Res. Bull.*, 2017, **86**, 63–71.
- 36 S. Huang, Z. Wei, X. Wu and J. Shi, *J. Alloys Compd.*, 2020, **825**, 154004.
- 37 N. Pathak, P. S. Ghosh, S. Saxena, D. Dutta, A. K. Yadav, D. Bhattacharyya, S. N. Jha and R. M. Kadam, *Inorg. Chem.*, 2018, **57**, 3963–3982.
- 38 D.-L. Ge, Y.-J. Fan, C.-L. Qi and Z.-X. Sun, *J. Mater. Chem. A*, 2013, **1**, 1651–1658.
- 39 M. Jain, Manju, A. Gundimeda, A. Kumar, S. Kumar, G. Gupta, S. O. Won, K. H. Chae, A. Vij and A. Thakur, *J. Alloys Compd.*, 2019, **797**, 148–158.
- 40 P. Tarte, *Spectrochim. Acta, Part A*, 1967, **23**, 2127–2143.
- 41 J. A. van Bokhoven, H. Sambe, D. E. Ramaker and D. C. Koningsberger, *J. Phys. Chem. B*, 1999, **103**, 7557–7564.
- 42 T. Dudev and C. Lim, *J. Am. Chem. Soc.*, 2000, **122**, 11146–11153.
- 43 D. Zhang, X. Ma, Q. Zhang, Y. Xie, Q. Shi, Q. Wang and W. Wang, *J. Alloys Compd.*, 2016, **688**, 581–587.
- 44 J. Vonhoene, R. G. Charles and W. M. Hickam, *J. Phys. Chem.*, 1958, **62**, 1098–1101.
- 45 Q. J. Jia, J. F. Zeng, R. R. Qjao, L. H. Jing, L. Peng, F. L. Gu and M. Y. Gao, *J. Am. Chem. Soc.*, 2011, **133**, 19512–19523.
- 46 Y. Zeng, W. Zheng, Y. Guo, G. Han and Y. Yi, *J. Mater. Chem. A*, 2020, **8**, 8323–8328.
- 47 T. Lu and F. Chen, *J. Comput. Chem.*, 2012, **33**, 580–592.